Development and translational imaging of a *TP53* porcine tumorigenesis model

Jessica C. Sieren,[1,2] David K. Meyerholz,[3] Xiao-Jun Wang,[4] Bryan T. Davis,[4] John D. Newell Jr.,[1] Emily Hammond,[1] Judy A. Rohret,[4] Frank A. Rohret,[4] Jason T. Struzynski,[4] J. Adam Goeken,[3] Paul W. Naumann,[3] Mariah R. Leidinger,[3] Agshin Taghiyev,[5] Richard Van Rheeden,[5] Jussara Hagen,[6] Benjamin W. Darbro,[2,5] Dawn E. Quelle,[2,3,6] and Christopher S. Rogers[4]

[1]Radiology and Biomedical Engineering, University of Iowa, Iowa City, Iowa, USA. [2]Holden Comprehensive Cancer Center, Iowa City, Iowa, USA. [3]Department of Pathology, University of Iowa, Iowa City, Iowa, USA. [4]Exemplar Genetics, Sioux Center, Iowa, USA. [5]Department of Pediatrics and [6]Department of Pharmacology, University of Iowa, Iowa City, Iowa, USA.

Cancer is the second deadliest disease in the United States, necessitating improvements in tumor diagnosis and treatment. Current model systems of cancer are informative, but translating promising imaging approaches and therapies to clinical practice has been challenging. In particular, the lack of a large-animal model that accurately mimics human cancer has been a major barrier to the development of effective diagnostic tools along with surgical and therapeutic interventions. Here, we developed a genetically modified porcine model of cancer in which animals express a mutation in *TP53* (which encodes p53) that is orthologous to one commonly found in humans (R175H in people, R167H in pigs). *TP53*$^{R167H/R167H}$ mutant pigs primarily developed lymphomas and osteogenic tumors, recapitulating the tumor types observed in mice and humans expressing orthologous *TP53* mutant alleles. CT and MRI imaging data effectively detected developing tumors, which were validated by histopathological evaluation after necropsy. Molecular genetic analyses confirmed that these animals expressed the R167H mutant p53, and evaluation of tumors revealed characteristic chromosomal instability. Together, these results demonstrated that *TP53*$^{R167H/R167H}$ pigs represent a large-animal tumor model that replicates the human condition. Our data further suggest that this model will be uniquely suited for developing clinically relevant, noninvasive imaging approaches to facilitate earlier detection, diagnosis, and treatment of human cancers.

Introduction

The need for immediate and rapid progress in cancer detection, diagnosis, and treatment is apparent, with 1 of every 4 deaths in the United States resulting from cancer (1). Despite recent technological and pharmaceutical advancements, effective treatment strategies for many forms of cancer remain elusive. Ideally, methods to detect the very early stages of tumorigenesis would allow rapid, effective therapeutic intervention to ablate existing cancer cells and prevent tumor progression. Medical imaging modalities (i.e., computed tomography [CT], magnetic resonance imaging [MRI], and positron emission tomography [PET]) play important roles not only in detection of tumors, but also in discrimination of benign from malignant disease, treatment response evaluation, and screening for metastatic disease. Advancements in medical imaging technology, applications, and comprehensive validation of clinical utility are needed to significantly improve cancer mortality rates. Unfortunately, there are challenges associated with research in human cancer subjects, including varied genetics and population demographics, differing treatment strategies, and limited access to tissues for histopathological validation.

Nonhuman tumor models are the most feasible platform to develop new and improved imaging approaches for noninvasive cancer detection and monitoring. Murine models are the most commonly used species in cancer research; however, they typically do not reflect the heterogeneity of disease observed in humans (2), and the microimaging systems developed to study murine models lack the capabilities of current clinical imaging systems (3). Large animals, such as dogs and pigs, have been used to develop new CT imaging protocols for translation to human subjects (4–6) and improving the clinical capabilities to characterize early stages of disease (7). However, use of large animal species in cancer research has been limited, with most examples being spontaneous, incidental cancers in companion and livestock animals. Efforts have begun to move cancer-modeling technology previously developed in mice to new species. For example, xenograft models are being tested in immunodeficient pigs (8), and several groups, including our own in the present study, are using gene engineering technology to introduce cancer-related mutations to the porcine genome (9, 10).

TP53 (which encodes p53) is the most commonly inactivated gene in sporadic human cancers (11), and it is also mutated in the germline of Li-Fraumeni patients who are strongly predisposed to developing multiple types of cancers. It is estimated that p53 function is compromised in the vast majority of human tumors, through either *TP53* gene mutation or alterations targeting the numerous regulators of p53 signaling (11–14). The primary role of p53 is to transcriptionally regulate genes involved in cell proliferation, apoptosis, DNA repair, autophagy, metabolism, and other critical processes

Authorship note: Jessica C. Sieren and David K. Meyerholz contributed equally to this work.
Conflict of interest: Xiao-Jun Wang, Bryan T. Davis, Judy A. Rohret, Jason T. Struzynski, Frank A. Rohret, and Christopher S. Rogers are employees of Exemplar Genetics, a company that has applied for a patent related to the work reported herein.
Submitted: February 14, 2014; **Accepted:** June 19, 2014.
Reference information: *J Clin Invest*. 2014;124(9):4052–4066. doi:10.1172/JCI75447.

Table 1. Gene targeting and somatic cell nuclear transfer summary

	Gene targeting efficiency[A]	Number of transfers	Embryos per transfer (average)	Pregnancy rate[B]	Live pigs per litter
Male	1.1%	3	130	67%	3
Female	1.0%	4	130	75%	8

[A]Percentage of G418^R clones that were properly targeted, as determined by PCR. [B]Refers to full-term gestation.

that maintain genomic integrity of cells following genotoxic insults, thereby preventing tumorigenesis and metastasis (11). The majority of the cancer-associated mutations in p53 impair its binding to DNA, including the R175H "hot-spot" mutation, which occurs in Li-Fraumeni patients and is one of the most frequent missense mutations in sporadic tumors (15–17). Various *TP53* mutations, including R175H, have been modeled in mice, which develop the expected range of tumors, including carcinomas, soft tissue and bone sarcomas, leukemia, and glioblastoma multiforme (18–21). However, there is a lack of genetically defined large-animal models of cancer that would be more ideally suited to longitudinal studies of tumor initiation, progression, and metastasis, as well as tumor remission in response to treatment, involving technology designed for human application (e.g., medical imaging, radiation oncology, and surgery).

Here, we generated and characterized a novel gene-targeted porcine model of cancer in which the orthologous R175H mutation (R167H in pigs) was introduced into the endogenous *TP53* alleles. These *TP53*$^{R167H/R167H}$ animals developed a spectrum of tumor lineages that mimicked those seen in humans with Li-Fraumeni syndrome and in mice expressing the same *TP53* mutation. Importantly, the potential value and feasibility of clinical imaging approaches, including CT and MRI, to detect and monitor tumor formation was validated.

Results

Targeted mutation of TP53 in porcine fetal fibroblasts. Gene targeting was used to introduce the R167H missense mutation in the endogenous *TP53* gene. The *TP53* R167H targeting vector was delivered into male and female fibroblasts harvested from Yucatan miniature pig fetuses using recombinant adeno-associated virus (rAAV) (Figure 1A, left). A similar approach was previously used to target porcine *CFTR* (22). After rAAV infection and antibiotic selection, a PCR screen identified 29 *TP53*-targeted cell lines (Figure 1A, middle). An allele-specific Southern blot confirmed that 24 of the PCR-positive clones also contained the intended R167H mutation (Figure 1A, middle), and overall gene targeting efficiencies of approximately 1% were achieved in both male and female cells (Table 1). A subset of PCR-positive, R167H-containing cells was selected for further characterization. Southern blots hybridized with *TP53*- and *Neo*^{R}-specific probes confirmed proper *TP53* targeting and absence of random integration (Figure 1A, right). Furthermore, the intended recombination event was verified by DNA sequencing.

Production of TP53-targeted pigs. *TP53*$^{R167H/+}$ cells were used as nuclear donors for somatic cell nuclear transfer (23). We performed a total of 7 embryo transfers (3 with male embryos, 4 with female embryos). These produced 5 full-term pregnancies resulting in 16 male and 29 female *TP53*$^{R167H/+}$ pigs (Figure 1B, left). PCR, Southern blot, and DNA sequencing were used to confirm the expected genotypes (Figure 1B, middle and right).

Upon reaching sexual maturity, *TP53*$^{R167H/+}$ males and females were mated, producing several litters whose genotypes were confirmed by PCR and genomic Southern blot (Figure 1C). We studied the offspring from 3 of the resulting litters, which contained 2 *TP53*$^{+/+}$, 7 *TP53*$^{R167H/+}$, and 6 *TP53*$^{R167H/R167H}$ pigs. While this limited number of litters did not contain the expected Mendelian inheritance pattern, χ^2 analysis of genotypes from subsequent litters (now totaling 68 pigs) fit a 1:2:1 ratio.

Functional inactivation of the porcine p53-R167H mutant protein. Wild-type p53 is kept at low levels by one of its own transcriptional targets, the Mdm2 E3 ubiquitin ligase, to allow for normal cell survival and proliferation (24, 25). In response to various cellular stresses, such as DNA damage or oncogene activation, the p53 protein becomes stabilized and transactivates genes that induce growth arrest or apoptotic cell death (11, 26). This ensures the repair of damaged DNA before cells divide or the removal of genetically compromised cells by apoptosis (Figure 2A). By comparison, *TP53* mutants such as human R175H (mouse R172H) are defective for wild-type p53 transcriptional function and accumulate to high levels in tumor cells due to loss of Mdm2 regulation (17, 18, 27). Failed induction of cell cycle–inhibitory genes, such as the cyclin-dependent kinase inhibitor *CDKN1A* (encoding p21; also known as *Cip1* and *WAF1*), also abolishes normal checkpoint arrest by mutant p53. As a consequence, p53 mutant cells continue to cycle improperly and divide in the face of DNA damage. This initially causes greater genetic mutation and cell death, but ultimately leads to the outgrowth of genetically altered survivors that promote tumorigenesis (Figure 2A).

We tested whether porcine p53-R167H behaves like its human and mouse orthologs by analyzing its expression and activity in primary pig fetal fibroblasts in the absence or presence of drug-induced DNA damage. As expected, mutant p53-R167H protein was more stable and highly expressed than wild-type protein under basal conditions (Figure 2B). DNA damage by doxorubicin treatment caused robust induction of p21 by wild-type p53 that coincided with G1 and G2 phase arrest of cells (Figure 2C). In contrast, dose-dependent loss of p21 induction and G1 phase arrest, along with an increase in apoptotic cell death (<2N DNA content), was seen in doxorubicin-treated cells expressing 1 or 2 alleles of p53-R167H (Figure 2, B and C). Similar in vitro findings have been reported for independently generated porcine fibroblasts expressing inducible *TP53*$^{R167H/R167H}$ alleles (10).

In normal cells expressing wild-type p53, mutagenic activation of RAS or other oncogenes provokes a permanent p53-mediated cell cycle arrest called senescence that protects cells from chromosomal instability and oncogenic transformation (Figure 2D and refs. 11, 28). In contrast, *TP53* mutation impairs its induction of senescence genes, such as *CDKN1A*, and allows cells to continue proliferating and acquiring genetic alterations in the face of mutant RAS expression. Consistent with those findings in mouse

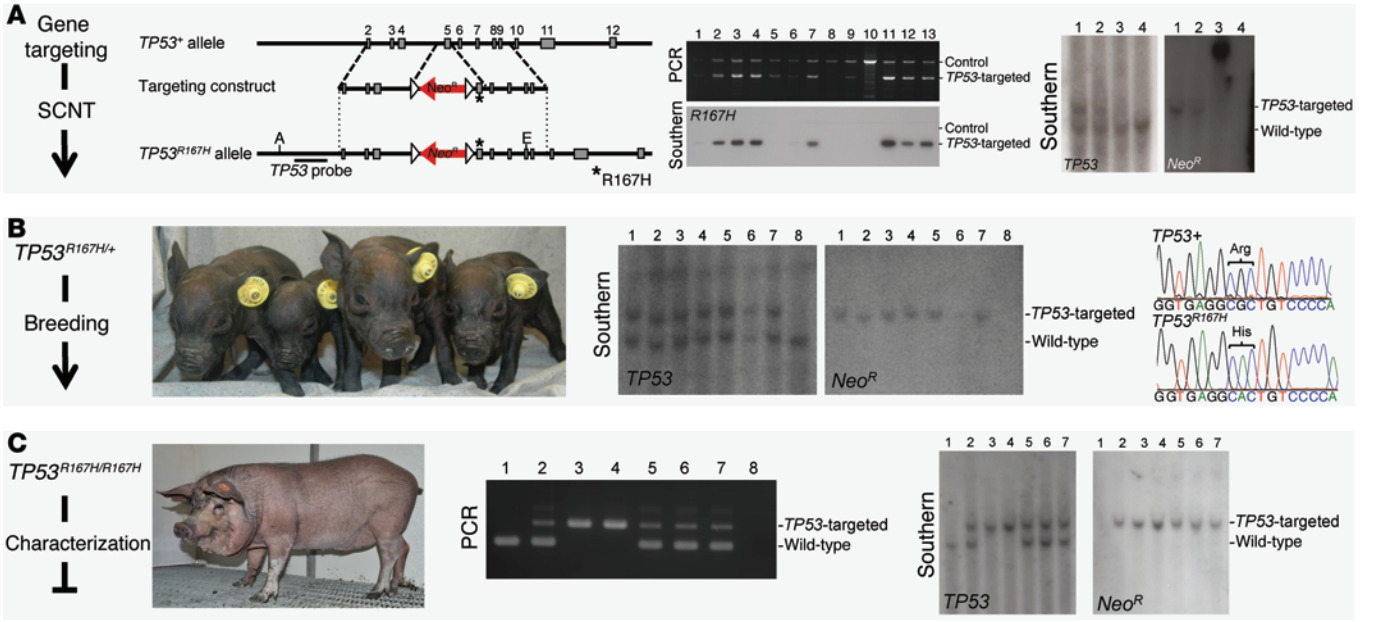

Figure 1. Production of *TP53*-targeted pigs. (**A**) Gene targeting via homologous recombination was used to introduce the R167H mutation in the endogenous *TP53* gene (left). AflII (A) and EcoNI (E) sites and *TP53* Southern blot probe are shown. PCR screen identified potentially targeted cell clones, and a biotin-labeled, allele-specific probe identified those contained the R167H mutation (middle). Amplified genomic DNA Southern blots confirmed properly targeted $TP53^{R167H/+}$ cell clones (right). (**B**) $TP53^{R167H/+}$ pigs were produced using somatic cell nuclear transfer (left). Genotypes were confirmed by genomic Southern blot (middle) and DNA sequencing (right). (**C**) A cross of $TP53^{R167H/+}$ males and females produced $TP53^{R167H/R167H}$ pigs (left), with genotypes being confirmed by PCR (middle) and genomic Southern blot (right).

and human cells, pig fibroblasts expressing 1 or 2 $TP53^{R167H}$ alleles effectively escaped mutant H-RAS–induced senescence (Figure 2, E and F, and Supplemental Figure 1; supplemental material available online with this article; doi:10.1172/JCI75447DS1). Wild-type cells infected with human $H\text{-}RAS^{G12V}$ viruses expressed increased p21, became fully arrested, adopted the flattened and enlarged morphology of senescent cells, and expressed high levels of senescence-associated β-galactosidase (SA-βgal) relative to vector controls, as expected (Figure 2, E and F, and Supplemental Figure 1). By comparison, cells expressing 2 alleles of mutant *TP53* continued to proliferate, failed to induce p21, were devoid of SA-βgal activity, and displayed no morphological features of senescent cells in response to mutant H-RAS expression. R167H-heterozygous fibroblasts exhibited an intermediate phenotype. Notably, $H\text{-}RAS^{G12V}$ expression still had the ability to slow down the proliferation of p53 mutant cells (Supplemental Figure 1C), likely due to induction of the cell cycle inhibitor $p16^{INK4a}$ (28). Together, these analyses confirmed that the porcine p53-R167H mutant protein was functionally defective in mediating DNA damage and oncogene checkpoints, similar to its human and mouse counterparts.

Tumor development in $TP53^{R167H/R167H}$ pigs. $TP53^{R167H/R167H}$, $TP53^{R167H/+}$, and $TP53^{+/+}$ pigs were monitored with a combination of clinical evaluation, peripheral blood analysis, in vivo CT and MRI, histopathology, and genetic characterization. The human-like size of this Yucatan miniature pig model enabled the use of clinical imaging technology and protocols (CT and MRI) for the longitudinal monitoring of tumorigenesis in this cohort. Supplemental Table 1 provides a summary of the pigs that underwent necropsy, including age at necropsy, clinical signs, and type of tumors detected. In addition to these necropsied animals, 7 $TP53^{R167H/+}$ and 5 $TP53^{+/+}$ pigs were monitored with in vivo imaging for tumor development. No tumors were detected via in vivo imaging or necropsy in the $TP53^{R167H/+}$ or $TP53^{+/+}$ cohort over 30 months of observation. Continued monitoring of the cohort is being conducted to determine whether tumors do develop in $TP53^{R167H/+}$ pigs at an advanced age.

All $TP53^{R167H/R167H}$ pigs that reached sexual maturity developed neoplastic lesions, including lymphomas, osteogenic tumors, and a renal tumor. However, 1 pig (case 1) in the first litter of $TP53^{R167H/R167H}$ pigs died 2 hours after birth. The necropsy did not reveal any discreet tumors, although the liver did have microscopic evidence of hepatocellular atypia (Supplemental Figure 2). Although no other pigs in our cohort displayed similar atypia or overt tumors in any livers, *TP53* mutations are associated with hepatocellular carcinoma (29); therefore, future phenotypic studies of the model will help determine whether this represents a precursor lesion for hepatocellular tumors.

In the $TP53^{R167H/R167H}$ cohort, 3 cases of lymphoma were identified and confirmed histopathologically (cases 2–4), with necropsy occurring over a range of 27–43 weeks of age. In vivo CT and MRI data collected for case 4 showed lymphadenomegaly consistent with lymphoma 16 weeks prior to necropsy (27 weeks of age; Figure 3). We observed enlargement of the liver and spleen, both indicators of possible diffuse infiltration of the liver with neoplastic lymphocytes (30, 31); thus, further examination of these organs was performed. The volume of the liver in $TP53^{R167H/R167H}$ case 4, as assessed by CT,

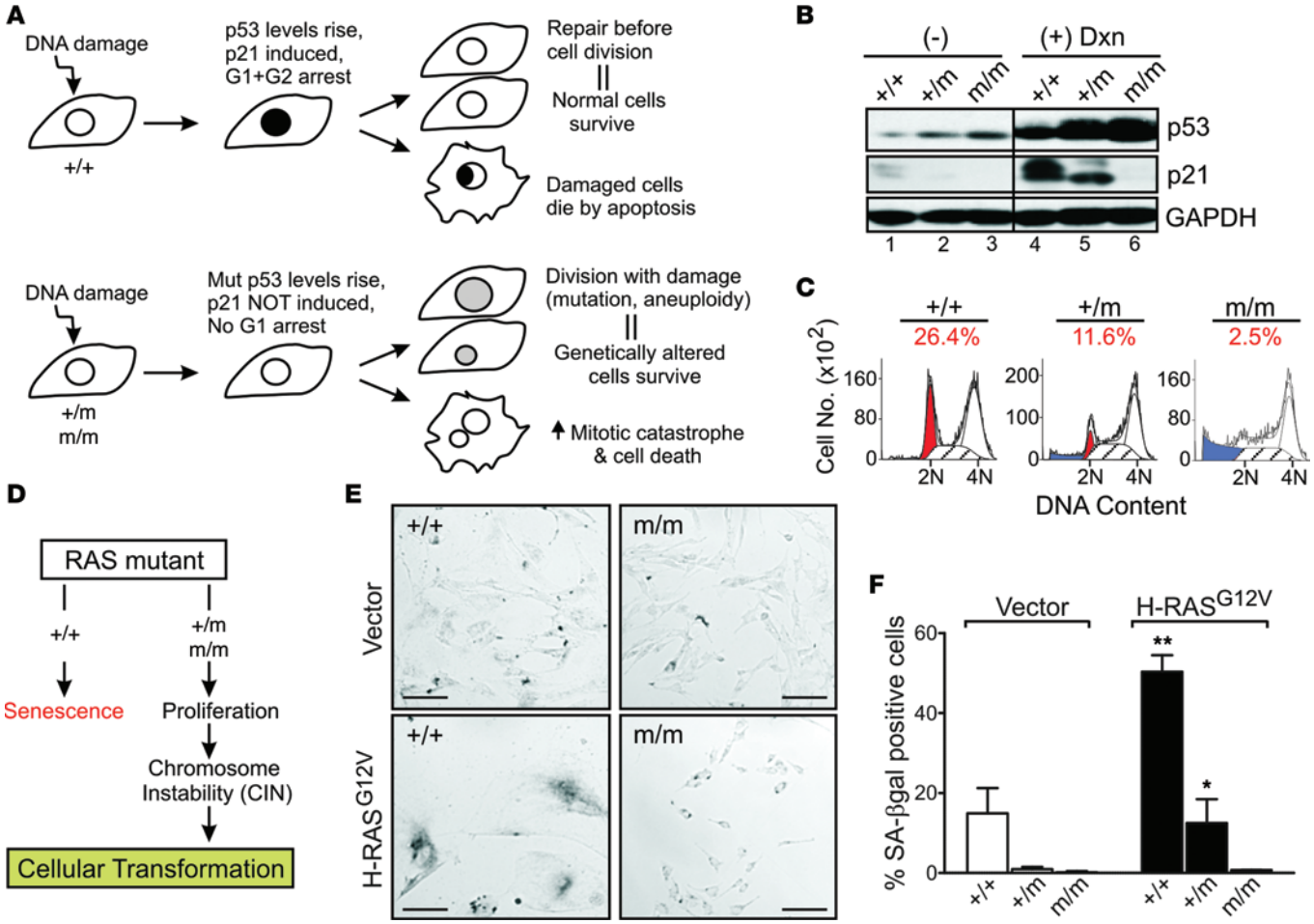

Figure 2. Defective molecular and biological activity of the porcine p53-R167H mutant protein. (**A**) Known differential response of cells expressing wild-type p53 (+/+) and mutated p53-R167H alleles (+/m or m/m) to DNA damage. Figure adapted with permission from *Nature* (26). (**B**) Western blots of p53, p21, and GAPDH (loading control) levels in p53 wild-type or R167 mutant pig fibroblasts. Cells were treated with DMSO vehicle (–) or 400 ng/ml doxorubicin (Dxn) for 3 days. Lanes were run on the same gel but were noncontiguous (black line). (**C**) Representative histograms of cell cycle distributions for doxorubicin-treated cells from **B**. Red, percent of cells arrested in G1 phase (2N DNA content); blue, cells undergoing apoptosis (<2N DNA content). (**D**) Mutant RAS induces cellular senescence in $TP53^{+/+}$ (+/+) cells, whereas $TP53^{R167H/+}$ (+/m) and $TP53^{R167H/R167H}$ (m/m) cells escape mutant RAS-induced senescence and proliferate, during which time they sustain chromosomal alterations that foster cell transformation. (**E** and **F**) Pig fibroblasts were infected with pBabe-puro vector or pBabe-H-RAS^{G12V}-puro viruses and selected with puromycin for 7–10 days. Shown are (**E**) phase-contrast microscopy and (**F**) counts of SA-βgal–stained cells. Cells expressing mutant p53 evaded senescence and proliferated, whereas those with wild-type p53 adopted the enlarged, flattened morphology of senescent cells and stained positively for SA-βgal. Data in **F** are mean ± SD of 3 independent experiments. Scale bars: 100 μm. $^*P < 0.05$, $^{**}P < 0.001$ vs. vector, 2-way ANOVA.

was found to be much larger than its weight-matched $TP53^{R167H/+}$ control (923 ml vs. 659 ml, respectively; Supplemental Figure 3I). The liver volume/animal weight ratio in $TP53^{R167H/R167H}$ case 4 was also larger compared with that in a $TP53^{R167H/+}$ cohort (26.4 ml/kg vs. 15.6 ml/kg, respectively). A mild elevation in quantitative CT–determined spleen volume was noted in the $TP53^{R167H/R167H}$ lymphoma case compared with the weight-matched $TP53^{R167H/+}$ pig (532 ml vs. 486 ml, respectively) and evidence of spleen enlargement was also reflected in the corresponding values of the spleen volume/animal weight ratio for the $TP53^{R167H/R167H}$ lymphoma case compared with the $TP53^{R167H/+}$ cohort (15.2 ml/kg vs. 13.5 ml/kg, respectively; Supplemental Figure 3I).

Elevated levels of contrast enhancement and delayed contrast clearance in both liver and spleen were observed by 3D fast gradient echo gadolinium-enhanced MRI imaging. Furthermore, quantitative assessment of the contrast-enhanced MRI study was performed comparing the liver/muscle and spleen/muscle MRI signal ratios. Both the liver/muscle ratio (1.13 vs. 0.89, respectively) and the spleen/muscle ratio (1.02 vs. 0.95 respectively) were increased in the $TP53^{R167H/R167H}$ lymphoma case compared with the weight-matched $TP53^{R167H/+}$ pig. Heterogeneity in signal enhancement in the organs in the $TP53^{R167H/R167H}$ lymphoma case compared with a weight-matched $TP53^{R167H/+}$ pig was reflected through calculation of the coefficient of variation in signal intensity in the spleen (27% vs. 14%, respectively) and liver (15% vs. 10%, respectively). Heterogeneous organ perfusion and delayed clearance of contrast media in the $TP53^{R167H/R167H}$ pig supported an imaging diagnosis of lymphoma.

At necropsy, enlargement of the lymph nodes and spleen were prominent and consistent features in affected $TP53^{R167H/R167H}$ pigs (Figure 3, B–E, and Supplemental Figure 3, A and B). Microscopically, sheets of neoplastic lymphocytes effaced tissue architecture

Table 2. Examples of imaging techniques linking to pathology findings in the *TP53*$^{R167H/R167H}$ pigs

Site	Imaging	Pathology
Case 5		
Cranium (R)	Right parasagittal lytic tumor (28 mm)	Extradural tumor composed of spindled to epitheloid cells that produced irregular trabeculae of osteoid (Supplemental Figure 4)
Sacrum (L)	Left side, lytic tumor (8 mm)	Large blood-filled chamber partially surrounded by dense bone and by loose connective tissue with cartilaginous/osteoid production (Supplemental Figure 5B)
Femur (L)	Distal metaphysis, lytic tumor (13 mm)	Solid sheets of tumor cells with scant osteoid production, but numerous multinucleate osteoclast-like cells (Figure 7)
Femur (L)	Proximal metaphysis, heterogeneous tumor (12 mm)	Dense osteoid/bone trabeculae extending from the edge of the cortex with a partial rim of osteosclerosis along periphery (Supplemental Figure 5C)
Tibia (R)	Diaphysis/metaphysis, hyperdense tumor (12 mm)	Tumor composed of coalescing bone trabeculae that effaced most of bone marrow to cortex (Supplemental Figure 5A)
Case 6		
Cranium (R)	Intracranial tumor extending into frontal sinus (39 mm)	Extradural tumor composed of spindled to epitheloid cells that produced irregular trabeculae of osteoid (Figure 5)
Femur (L)	Distal diaphysis/metaphysis, hyperdense tumor (18 mm)	Spindled cells on collagenous to mineralized matrix with a peripheral rim of osteosclerosis (Figure 6)
Tibia (L)	Proximal metaphysis, hyperdense tumor (13 mm)	Tumor composed of coalescing bone trabeculae lined by scattered loose connective tissue rare osteoblasts (Supplemental Figure 5)
Kidney (R)	Superior pole, hypodense tumor (26 mm)	Diffuse coagulation necrosis with hemorrhage; tumor had numerous irregular tubules with interspersed bands of connective tissue; scattered nests of poorly differentiated tubules invaded through capsule (Figure 8)
Mesentery	Irregular hyperdense tumor	Regional mesentery with irregular to elongate bony tumors composed of coalescing trabeculae of bone/osteoid; heterogeneity seen with focal proliferations to mature bone line by low cellularity connective tissue (Supplemental Figure 6)

L, left; R, right.

in these organs (Figure 3, D and E, and Supplemental Figure 3B), with extension into liver and lung (Supplemental Figure 3, E–H). In case 2, the animal died suddenly and had hemo-abdomen secondary to splenic rupture (Supplemental Figure 3, C and D). The lungs (and other organs) had vessels filled with abundant cellular and nuclear debris (Supplemental Figure 3, E and F), histologically consistent with tumor lysis syndrome, seen in many mouse models (32, 33) and in humans undergoing cytolytic cancer therapy (34, 35). Case 2 had routine blood work evaluated 2 days prior to its sudden death. At that time, the absolute lymphocyte count of case 2 was similar to or marginally increased compared with control littermates, but all these values were within the normal reference range ($3.3–11.5 \times 10^3$ cells/μl). This suggests that leukemia was not present and that the necrosis/rupture of the spleen in the hours prior to death was likely the mechanism for tumor cells and cellular debris to enter into the vasculature as emboli. All 3 *TP53*$^{R167H/R167H}$ lymphoma cases had changes in selected peripheral blood parameters compared with control animals in the final days prior to necropsy (Figure 4, A–D). Interestingly, a routine blood sample collected 2 days prior to necropsy did not distinguish case 2 from the other lymphoma cases (cases 3 and 4), which suggests that the tumor lysis syndrome was associated with acute splenic rupture as opposed to tumor burden.

Osteogenic tumors were also identified through in vivo imaging in 2 *TP53*$^{R167H/R167H}$ pigs (cases 5 and 6). CT and MRI detected a 28 mm right parasagittal, calvarial lytic (137 HU) tumor in case 5 at 53 weeks of age. The tumor expanded into the intracranial cavity and also caused destruction of adjacent bone tissue (Supplemental Figure 4). In vivo CT and MRI data collection was completed for case 6 at 2 time points. At 53 weeks of age (time point 1), osteogenic tumors in the long bones were detected, but no skull/calvarial tumor was present; at 60 weeks of age (time point 2; 51 days later), a 39 mm intracranial tumor was detected (Figure 5). The tumor infiltrated through the bony calvarium to invade both the frontal sinuses and the intracranial compartment, with evidence of extrinsic compression of the brain parenchyma. The tumor contained bony matrix, as indicated by increased CT attenuation (305 HU). This was supported by the heterogeneous signal enhancement present in the SPACE MRI data for both case 5 and case 6 calvarial tumors, indicative of areas of both soft tissue and calcification/ossification. Microscopically, the 2 calvarial tumors were composed of spindled to epitheloid cells that produced osteoid trabeculae (Figure 5 and Supplemental Figure 4). Both tumors had invasion, with the case 5 tumor infiltrating into the frontal sinus(es) (Figure 5, A–D). The sum of the imaging, histological, and biological features were consistent with osteosarcoma.

The microscopic lesions in the calvarial tumors were similar in appearance, whereas the other osteogenic tumors in these animals had a varied microscopic appearance, even within the same pig. These changes ranged from osteoid/bone-rich to osteoid-poor lesions with proliferative mesenchymal cells (Figures 6 and 7 and Supplemental Figures 5 and 6). These other osteogenic tumors were located in the tibia, femur, and sacrum, ranging in size from 8 to 18 mm (cases 5 and 6; Table 2). Lytic lesions presented with mean CT attenuations of 87–156 HU. Heterogeneous and hyperdense lesions ranged 307–927 HU in mean CT attenuation. The osteogenic tumors in the long bones of case 6 were all present at time point 1, prior to development of the calvarial tumor. No significant change in tumor size was detected for any of the osteogenic tumors of the long bones, while some subtle changes in CT

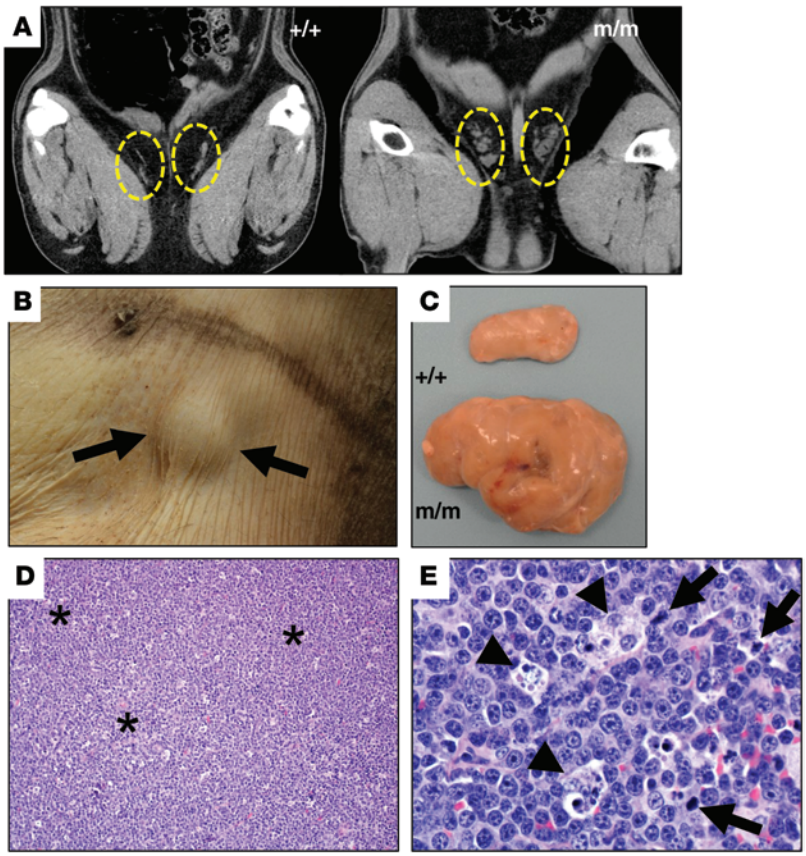

Figure 3. Lymphoma in *TP53*$^{R167H/R167H}$ pigs. Early-stage enlargement in inguinal lymph nodes were detected. (**A**) Coronal CT cross-sections illustrating the difference in lymph node short axis size: 26 mm in *TP53*$^{R167H/R167H}$ (case 3) relative to 9 mm in *TP53*$^{+/+}$ (case 7). Image data were acquired 4 months prior to necropsy at 27 weeks of age. (**B** and **C**) Lymphadenopathy was a consistent finding upon external examination (arrows, **B**; case 3) and at necropsy (**C**; case 6). (**D**) Lymph nodes were consistently effaced by sheets of neoplastic lymphocytes (asterisks; case 3). (**E**) Microscopically, the neoplastic lymphocytes had numerous mitotic figures (arrows) and frequent tingible body macrophages (arrowheads). Original magnification, ×100 (**D**); ×600 (**E**).

attenuation were observed, such as the increased solid component of the tumor in Figure 6. Importantly, no osteogenic tumors were seen in long bones of the pigs without osteosarcoma tumors (littermate *TP53*$^{R167H/R167H}$, *TP53*$^{R167H/+}$, and *TP53*$^{+/+}$ pigs).

In one of the *TP53*$^{R167H/R167H}$ pigs with osteogenic tumors (case 6), a renal tumor was also detected via CT and MRI imaging (Figure 8, A–D). The tumor (25.8 mm; 8.9 ml) was located in the right cranial pole of the kidney, with an accompanying focus of hemorrhage (23.4 ml), at time point 1. Image data of the tumor at time point 2 showed nominal changes in tumor size (26.3 mm; 7.1 ml), but had obvious resolution of the hemorrhage component. Contrast-enhanced CT attenuation of the tumor decreased from time point 1 to time point 2 (62 HU to 55 HU, respectively), reflecting an increase in necrotic tissue component, which was supported by histopathology findings (Figure 8, E and F).

Signal intensity in the tumor relative to the unaffected renal cortex was assessed within the MRI data. Precontrast, T1-weighted (VIBE) MRI data revealed a shift from time point 1 to time point 2 from isointense to hypointense signal relative to the renal cortex. The hemorrhage in time point 1 was clearly evident as a hyperintense component. Postcontrast, T1-weighted (VIBE) MRI demonstrated a heterogeneous enhancement at time point 1 and a decrease in signal intensity relative to the renal cortex at time point 2. The resolution of the hemorrhage component and increase in necrosis between the time points is likely responsible for the relative decrease in signal intensity in the follow-up postcontrast MRI data.

Microscopically, the renal tumor was composed of necrotic tubules and intervening cords of connective tissue and foci of hemorrhage (Figure 8, E and F). Within and extending through the tumor capsule were small, invading nests of poorly differentiated tubules that had a high mitotic rate (Figure 8, E and G). The imaging and pathological findings were consistent with a Wilms tumor (nephroblastoma), a malignancy commonly associated with p53 pathway perturbations in which *TP53* mutation correlates with a less favorable prognosis (36–38).

In addition, a mesenteric tumor was detected for case 6 (Supplemental Figure 6). The tumor shape was highly irregular and spiculated, with high mean CT attenuation compared with the surrounding soft tissues (472 HU vs. 30–50 HU, respectively). A significant growth in tumor volume from 2.07 ml to 3.08 ml (48% increase) was measured from imaging time point 1 to time point 2, with minimal change in mean CT attenuation (+2 HU). At necropsy, the irregularly shaped bony tumor was located within the mesentery (Supplemental Figure 6). The location of the bony mesenteric tumor was near the site of hemorrhage from the renal tumor (Figure 8); this and its general appearance were consistent with mesenteric myositis ossificans (Supplemental Table 2).

Molecular genetic analyses of TP53$^{R167H/R167H}$ *tumors*. Several excised lymph nodes and osteogenic tumors were subjected to Western blot analyses to confirm p53-R167H mutant protein expression and activity. Compared with the essentially undetectable expression of nonmutated p53 from wild-type pig brain tissue, mutant p53-R167H protein was expressed at higher levels in each malignant sample (Figure 9A), as anticipated. The porcine p53-R167H mutation, like its human (R175H) and mouse (R172H) counterparts, is expected to behave as a gain-of-function mutant that fails to regulate normal p53 transcriptional targets (such as p21; see Figure 2 and Supplemental Figure 1B) and instead transactivates a new set of oncogenic gene targets, including cyclin B1 (17, 39). Indeed, tumors and lymph nodes expressing p53-R167H showed marked upregulation of cyclin B1 protein (Figure 9A). Human tumors expressing mutant p53 primarily sustain chromosomal alterations as opposed to genomic sequence mutations (40). We conducted cytogenetic analyses of metaphases from a lymph node and osteosarcoma isolated from *TP53*$^{R167H/R167H}$ pigs, which revealed significant abnormalities in both chromosome number and structure (Figure 9, C and D). In contrast, a normal karyotype was seen in the skin tissue of a wild-type pig control (Figure 9B). These findings confirm the altered expression and activity of mutant p53-R167H in the

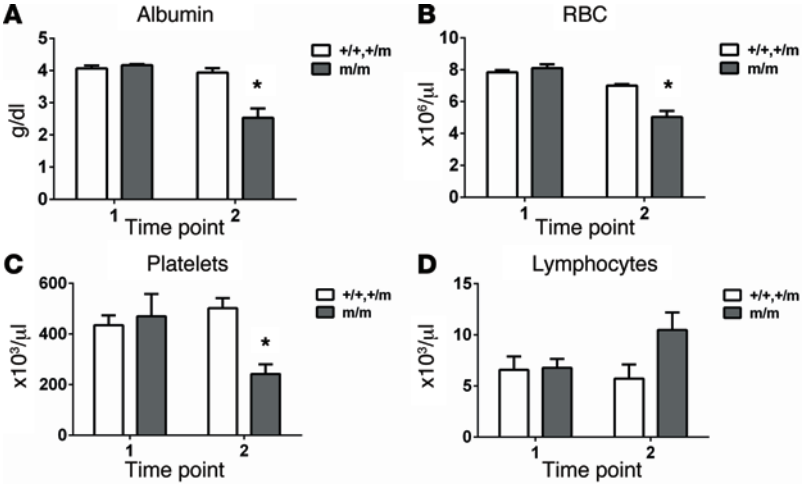

Figure 4. Peripheral blood parameters. Nondiseased control (cases 7, 9, and 10) and lymphoma cases (cases 2–4) in *TP53*$^{R167H/R167H}$ pigs were examined ~4–6 weeks prior to (time period 1) and the week of (time period 2) euthanasia/death. *TP53*$^{R167H/R167H}$ pigs were similar to nondiseased controls at time period 1, but had significant decreases compared with controls in albumin ($P < 0.001$; **A**), red blood cells ($P < 0.001$; **B**) and platelets ($P < 0.05$; **C**) at time period 2. (**D**) Lymphocyte counts were similar in *TP53*$^{R167H/R167H}$ and control pigs at time period 1, but by time point 2 there was a nonsignificant trend toward increased numbers in the *TP53*$^{R167H/R167H}$ animals. *$P < 0.05$, 2-way repeated-measures ANOVA with Bonferroni post-test.

TP53$^{R167H/R167H}$ tumors, as well as the characteristic chromosomal instability known to accompany *TP53* mutation in human tumors.

Discussion

Large animals are becoming increasingly relevant for modeling human diseases, especially for cases in which body size and lifespan are important. This is particularly true for cancer, for which imaging technologies and surgical procedures are instrumental in current detection and treatment plans. Conventional small-animal models such as mice have inherent limitations, including a body size approximately 1:1,000 that of humans and a lifespan of only 1–2 years. To address the lack of a suitable large-animal model of cancer, we mutated the porcine *TP53* gene and generated pigs with lymphoma, renal, and osteogenic tumors. Importantly, clinically relevant imaging techniques were used to identify each tumor type and direct the postmortem collection of samples for histopathological and molecular analyses. During the course of the present study, another group reported a similar gene modification in domestic pigs; however, no cancer was described (10). To our knowledge, the *TP53* mutant pigs described here are the first gene-targeted large animals with confirmed cancer development.

Advantages of the porcine cancer model. Specific attributes of the porcine model offer new research opportunities that are not feasible in current cancer models; 2 prime examples are size and lifespan. We chose to develop the mutant *TP53* model in the Yucatan miniature pig, a breed that reaches a full-grown weight of 60–75 kg at 2 years of age, similar to that of an adult human. This makes it better suited than small-animal models for studies involving the optimization and validation of imaging technologies and surgical procedures. It is important to note that a model can also be too large. For example, domestic pig breeds, such as those being used in other cancer models (8–10), are 2–3 times bigger. This would exclude domestic pigs from most longitudinal monitoring/treatment studies with clinical imaging technologies, as they would quickly outgrow the size capacity of a typical clinical imaging scanner with a bore diameter of 60–70 cm. Also related to size, as opposed to small-animal models, tissues from Yucatan miniature pigs are available in sufficient quantities to develop porcine tissue repositories containing cancer and matched normal tissues for future studies. Likewise, the larger circulatory volume of Yucatan miniature pigs compared with mice permits more repeated sampling of peripheral blood for potential biomarkers of cancer, enabling a broader spectrum of disease parameters to be monitored over time. Finally, the lifespan of pigs (10–15 years) is quite long compared with other animal models, facilitating investigations of the natural history of various cancers, long-term treatment effects, and successive surgical interventions.

A large-animal cancer model presents opportunities to improve clinical cancer outcomes in humans by serving as a controlled surrogate for human cancer patients. Consequently, research studies may be designed with a small target population of animals that may be studied extensively, with unrestricted access to validating tissue samples. Thus, large amounts of data, with tightly controlled cofactors and low population variation, may be achieved, requiring fewer subject numbers for equivalent statistical significance than a human cancer cohort. Furthermore, many cancer types are heterogeneous in content, composed not only of cancerous cells, but also of inflammatory mediators (41), fibrotic stroma (42), necrotic tissue, and complex vascularity (43). Our porcine model does not rely on an immunocompromised host for tumor development, unlike xenograft models (8). The mutant *TP53* pig opens new lines of investigation to explore the interplay between a functional immune response and the tumor microenvironment as it relates to tumor progression, diagnosis, treatment, and monitoring (44).

Applications of the porcine cancer model. The porcine cancer model provides new opportunities to improve cancer detection, monitoring, and treatment approaches in ways not possible with murine models or human patients. Medical imaging technologies (e.g., CT, MRI, and PET) play a key role in the clinical management of cancer patients in facilitating cancer detection, staging, and treatment response monitoring. However, the advanced capabilities of these systems are in many cases underutilized clinically, due to significant challenges in protocol optimization and validation within the cancer patient population (45). A large-animal cancer model allows for the collection of many imaging datasets with varying protocols and modalities in the same cancerous tumor. Thus, image data features can be directly compared, and optimal protocols and/or modalities may be identified. This capability would be highly useful in the optimization of radiation dose, con-

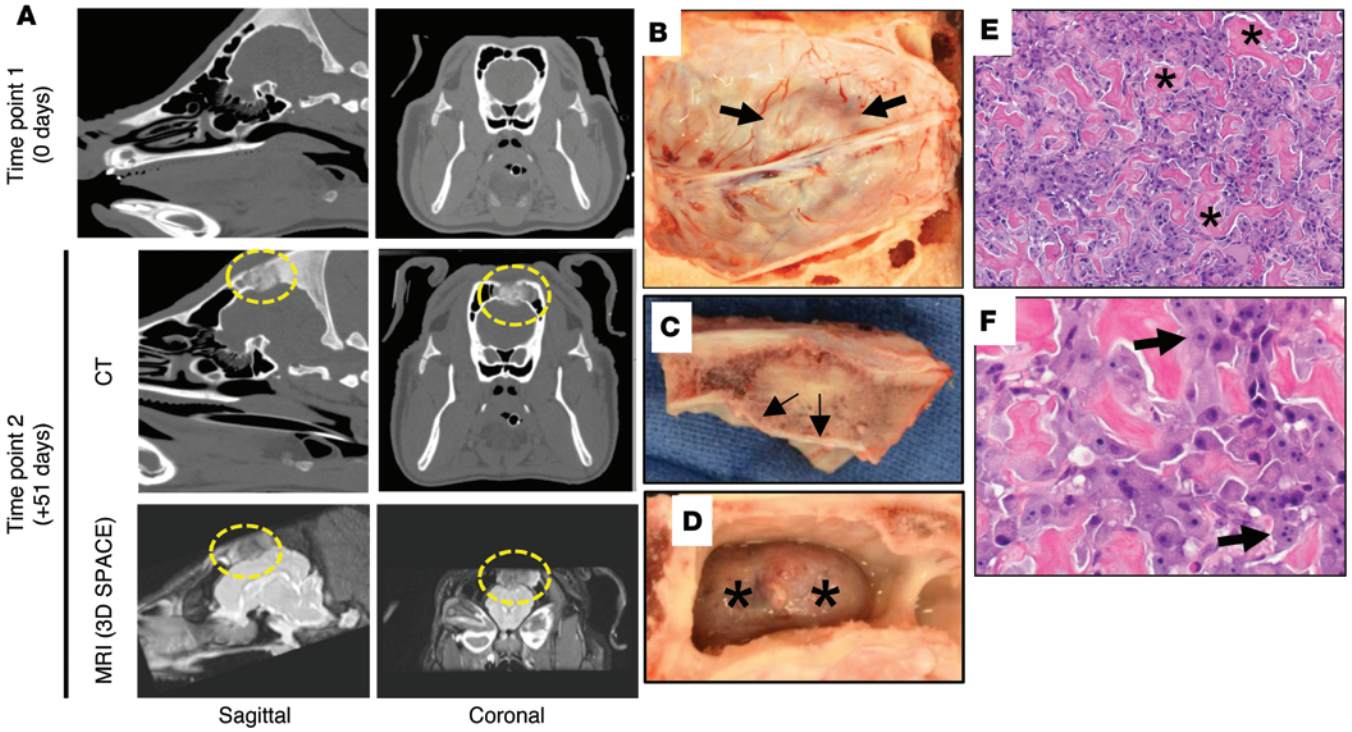

Figure 5. Osteogenic tumor a in a *TP53*$^{R167H/R167H}$ pig. In vivo imaging of case 6 with CT, showing coronal and sagittal cross-sectional views. (**A**) Whereas views from time point 1 showed no evidence of tumor lesion, views from time point 2 in CT and MRI (51 days later) revealed aggressive tumor growth (39 mm). (**B** and **C**) The extradural mass (arrows, **B**) expanded into the cranial vault (arrows, **C**), compressing the brain. (**D**) The mass (asterisks) invaded into the frontal sinus cavity. (**E**) The calvarial mass was composed of round to spindle cells that produced irregular trabeculae of osteoid (asterisks). (**F**) The neoplastic cells had varying sized nuclei with a prominent nucleoli (arrows). Original magnification, ×200 (**E**); ×600 (**F**).

trast delivery rate, and scan delay timing for dynamic dual-energy CT (46). Comparison of alternate PET radiotracers, along with improved acquisition strategies to optimize PET resolution, would also benefit from a human-sized cancer model (47, 48).

While microimaging technology exists for CT, PET, and MRI data acquisition in murine cancer models, these systems do not contain the same capabilities of the equivalent clinical systems (3, 49). These differences in acquisition technology — combined with large differences in subject size as well as heart, respiratory, and metabolic rates — make rodents ineffective models for translatable protocol development. In a human cancer cohort for research, there is often a high degree of variability in cancer type and stage, clinical treatment approach, subject comorbidities, and access to endpoint data (e.g., mortality and comprehensive histopathology). There are also restrictions that limit the ability to acquire multiple data points, such as minimizing exposure to medical ionizing radiation, study time limitations, and primary concern for the patient's clinical treatment and survival. The porcine model overcomes these constraints.

Another important capability provided by the porcine cancer model is to use medical imaging technology to monitor cancer development over time, with or without intervention. Studying cancer progression in the absence of treatment is not possible in humans. In this porcine model, data may be collected prior to tumor development, during tumor growth, and through to metastatic disease. This will provide insight into cancer pathogenesis and the ability of current medical imaging technologies to capture and classify the changing states of cancer progression. Medical imaging is key in planning clinical interventions. The similar anatomy and physiology to humans makes this porcine model ideal to test image-guided, minimally invasive surgical techniques as well as intensity-modulated radiation therapy strategies (50). Comprehensive post-intervention evaluation in the porcine model is also feasible, using multimodality imaging and tissue resection to determine whether effective destruction of all cancer cells is achieved, whether early indicators of metastatic disease can be found in other target organs, and/or whether toxicity occurs in nondiseased tissue.

TP53 and cancer. *TP53* mutations, which occur in the majority of sporadic human cancers and some inherited cancer-prone disorders, compromise protective checkpoints in cells that normally ensure genomic integrity, thereby facilitating cellular transformation and tumorigenesis (11, 17). In the present study, all *TP53*$^{R167H/R167H}$ pigs that reached maturity developed some type of cancer, including lymphoma, Wilms tumor (nephroblastoma), and osteogenic tumors (osteosarcoma). Each tumor type is associated with mutations of *TP53* and/or its pathways in humans and is found in Li-Fraumeni patients expressing the p53-R175H mutant modeled in our *TP53*$^{R167H/R167H}$ pigs (51–53). The complete tumor penetrance obtained in *TP53*$^{R167H/R167H}$ pigs, and the corresponding lack of tumor development in wild-type control animals, indicates that the cancers arising in these pigs are due to *TP53* gene targeting and not spontaneous tumorigenesis, whose incidence for the tumor types observed is exceedingly low (between 2–20 per 100,000; refs. 54, 55).

The osteogenic tumors seen in *TP53*$^{R167H/R167H}$ pigs may be of particular clinical interest and relevance. While Li-Fraumeni

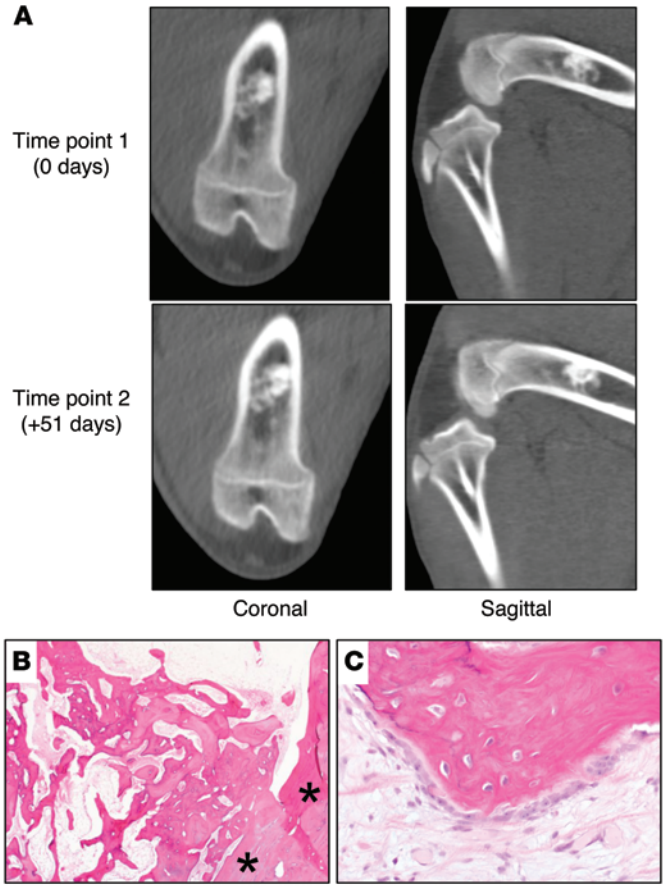

Figure 6. Osteogenic tumor in a *TP53*$^{R167H/R167H}$ pig. (**A**) Imaging of case 6 showed an 18 mm lesion in the left distal femur with heterogeneous CT density. Views at time point 2 showed growth in the solid component of the lesion compared with time point 1. (**B**) The tumor was composed of irregular trabeculae of osteoid and bone extending from the edge of the cortex (asterisks). (**C**) The bony trabeculae were at times lined by loose mesenchymal to fibrous tissue and uncommon rims of osteoblasts. Original magnification, ×20 (**B**); ×400 (**C**).

patients develop this type of tumor (51, 53), most osteosarcomas seen in humans actually arise sporadically and are associated with somatic *TP53* mutations (56), which correlates with greatly reduced event-free survival (57, 58). Importantly, while the clinical aspects of osteosarcoma are well defined (Supplemental Table 2 and ref. 59), the early pathogenesis of this malignancy is not well understood. A prior study of transformation from benign to malignant osteogenic tumors suggests that tumor progression is associated with an increased frequency of genetic alterations (60). Chromosome clonality (61) and *TP53* alterations (62) have been described in benign osteogenic tumors, and subsequent osteosarcoma arising from a benign osteogenic tumor has been reported (63). Here, the *TP53*$^{R167H/R167H}$ pigs had a wide spectrum of osteogenic tumors ranging from osteosarcoma of the calvaria to various low-grade/benign tumors (e.g., giant cell tumor of bone) of long bones. Metastases could explain the multiple osteogenic tumors in a single animal; however, the timing and biological appearance of tumors at calvarial versus appendicular sites, together with the lack of lymph node and pulmonary metastases, would suggest that these tumors are de novo in origin. It will be informative to study the clonality of these individual tumors and determine whether their biology and genetics change over time to match their progression to osteosarcoma, as is seen in humans. The ability to conduct broader interspecies comparisons among humans, mice, and now pigs should strengthen the probability of identifying common and potentially causative molecular events required for malignant conversion to osteosarcoma (64).

Limitations. Although the initial diagnostic characterization is promising, this model does possess some limitations. First, the spectrum of tumors thus far was restricted, in part, due to the experimental design of this study that prioritized detection and phenotypic assessment of the initial tumors in the model. Mouse models with nonfunctional p53 commonly have early clinical disease due to lymphoma, with an expanded range of sarcoma and carcinoma tumor types that develop over time. As more *TP53*-targeted pigs are studied over a longer time, we expect to observe progression of tumors already seen in this study, as well as development of additional tumor types frequently seen in humans and mice with *TP53* mutations. For example, although breast carcinomas are the most frequent tumor observed in Li-Fraumeni patients, we did not detect any in this initial cohort. Second, since the timing and location of tumor presentation in these pigs was random, longitudinal monitoring (e.g., imaging) may be required for some studies. Third, our detection and phenotypic evaluation of early tumorigenesis in the *TP53*-targeted pig model likely precluded development of metastases that occur in later stages of disease. Those issues notwithstanding, the mutant *TP53*-targeted pigs represent a powerful platform for developing other cancer models with conditional, tissue-specific tumors. Of great interest is modeling cancer types such as lung, ovarian, and pancreatic adenocarcinomas, in which earlier detection by innovative imaging and/or biomarker analyses should translate into marked improvements in clinical management and patient survival. In that regard, the mutant *TP53* heterozygous pigs were 30 months old at the end of the present study and lacked evidence of tumor development. We anticipate these animals will get tumors at a slower rate than the mutant *TP53* homozygotes. This delay provides an ideal window of time for examining cooperative tumorigenic effects of mutations to other cancer genes in the heterozygote *TP53* model. For example, we are currently pursuing models of several tumor types by adding conditional oncogene activation (e.g., *KRAS*) to the heterozygote *TP53* background. This strategy has been extremely successful in murine models (65, 66), and we anticipate that success will extend to pigs, as well.

Conclusion. In summary, we have generated a new large-animal model of cancer by targeting porcine *TP53*. Using translational protocols and techniques, we demonstrated that the porcine model recapitulated many aspects of human cancer development. We anticipate that porcine cancer models will provide a comparatively low-cost platform (relative to human studies) for optimizing tumor diagnostic methodologies, including novel imaging approaches that can be directly applied in the clinic. Indeed, these long-lived tumor models should address several unmet needs and provide new opportunities for longitudinal studies of tumorigenesis (e.g., initiation, progression, and response to treatment) that will ultimately improve our ability to detect and treat cancers earlier in humans.

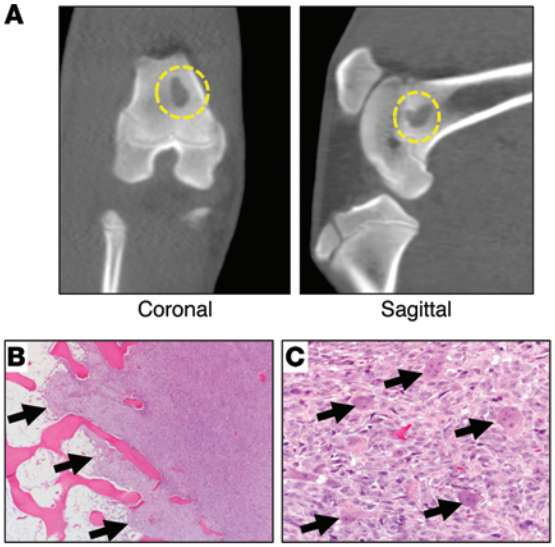

Figure 7. Osteogenic tumor in a *TP53*$^{R167H/R167H}$ pig. (**A**) In case 5, a 13 mm lytic tumor was identified by noncontrast CT in the left distal femur. (**B** and **C**) The tumor (arrows, **B**) effaced bone marrow (note absence of trabeculae at right edge, **B**) and was composed of sheets of pleomorphic round to spindle cells with scant osteoid deposition and multinucleate osteoclasts (arrows, **C**) were prominent within the tumor. Original magnification, ×40 (**B**); ×400 (**C**).

Methods

Fetal fibroblast isolation. Fetal fibroblasts were isolated from approximately day-35 Yucatan miniature pig fetuses using previously described methods (67). Cells were grown at 39°C and 5% CO_2 in F10 media (Invitrogen) containing 20% FCS and 30 μg/ml gentamicin. Fetus genders were previously identified by PCR amplification of the Y chromosome–specific *Sry* gene (68).

Cloning porcine TP53 genomic DNA. Genomic DNA was isolated from Yucatan fetal fibroblasts (Qiagen). A 7.1-kb PCR product, which included a region from *TP53* exon 2 to exon 11, was amplified using a high-fidelity polymerase (Platinum Taq High Fidelity; Invitrogen) and *TP53* primers GC2F and GC2R (see Supplemental Table 3 for all primer sequences). The PCR product was subcloned into pCR2.1-TOPO (Invitrogen) and sequenced. All DNA sequencing was performed by the University of Iowa DNA Facility. This plasmid (referred to as pTP53) served as the template for PCR amplification of the 5′ and 3′ homologous targeting arms.

Targeting vector construction. The 5′ and 3′ homologous recombination arms were amplified by PCR using plasmid pTP53 and subcloned sequentially into a plasmid containing a PGK-Neo cassette. The primers for the 5′ arm were pTP53 5′armF (EcoRV) and pTP53 5′armR (EcoRV). The primers for the 3′ arm were pTP53 3′armF (BamHI) and pTP53 3′armRv2 (HindIII). The R167H mutation was introduced using site-directed mutagenesis with primers R167H-F and R167H-R. This targeting construct (pTP53-Neo) was used as a template to create the amplicon for the generation of the *TP53*^{R167H}-targeting proviral vector.

rAAV production. PCR amplification of a 4.5-kb amplicon from plasmid pTP53-Neo was achieved using primers TP53-R167H-AAV-F (NotI) and TP53-R167H-R (NotI). This product was subcloned into the rAAV proviral plasmid, pFBAAV2-CMVP.NpA (obtained from University of Iowa Gene Transfer Vector Core), and grown in Sure2 cells (Stratagene) to ensure ITR integrity. This proviral plasmid is referred to as pAAV-TP53-R167H-Neo. The rAAV was produced by the University of Iowa Gene Transfer Vector Core.

Fetal fibroblast infection and selection. Passage-0 male and female Yucatan fetal fibroblasts (1.0×10^6) were thawed and plated on separate 100-mm collagen-coated culture dishes containing PFF media. Each cell line was infected with rAAV (18 μl, 4.65×10^{13} vg/ml) after 24 hours. Cells were subsequently detached with trypsin 24 hours

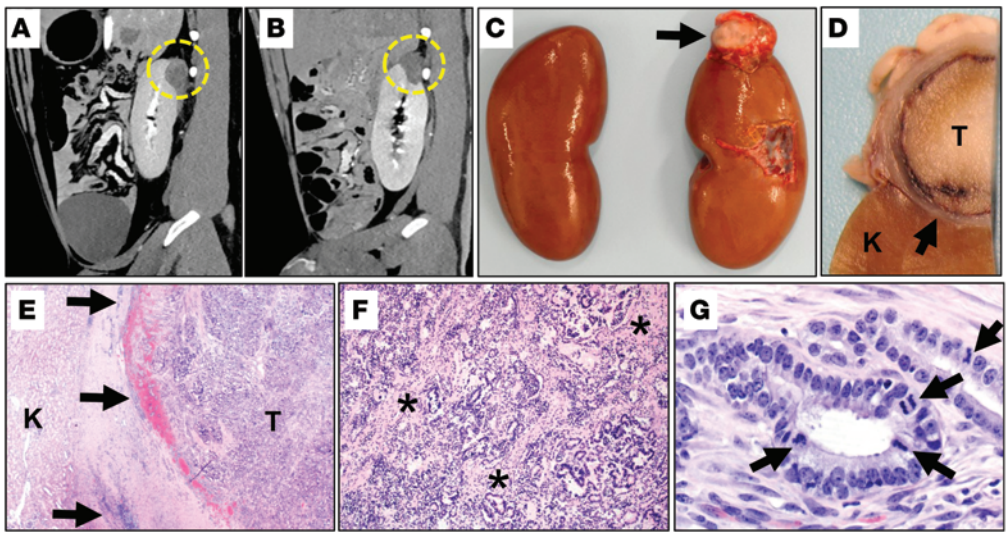

Figure 8. Renal tumor in a *TP53*$^{R167H/R167H}$ pig. In case 6, the change in renal tumor size over time was assessed with iodinated contrast-enhanced CT at time points 1 (**A**) and 2 (**B**); sagittal views are shown. (**C**) The renal tumor (arrow) was elevated from the cortex at the cranial pole of the right kidney. (**D**) Cut surface of the tumor (T) showed an encapsulated (arrow) mass that was well-demarcated from normal kidney (K). (**E**) The tumor was composed of necrosis and hemorrhages (red patches) that were distinct from the unaffected kidney. (**F**) The necrotic tumor tissue had irregular tubules separated by cords of connective tissue (asterisks). (**G**) At the edges of the tumor, invading through the tumor capsule were small nests (see **E**, arrows) of poorly differentiated tubules with a high mitotic rate (arrows). Original magnification, ×20 (**E**); ×100 (**F**); ×600 (**G**).

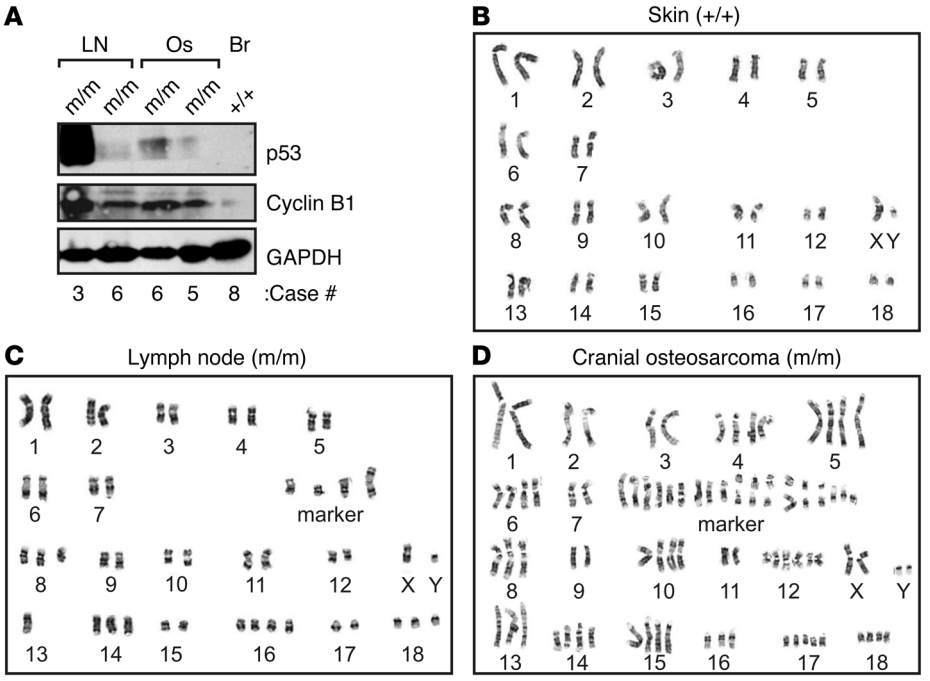

Figure 9. Molecular changes and cytogenetic abnormalities in *TP53*$^{R167H/R167H}$ pig tumors. (**A**) Western blots show increased expression of mutant p53-R167H protein and its transcriptional target, cyclin B1, in lymph nodes (LN) and osteogenic tumor (Os) from *TP53*$^{R167H/R167H}$ pigs (m/m), relative to low levels of each wild-type protein in the brain (Br) of normal *TP53*$^{+/+}$ pigs. GAPDH levels served as the loading control. The case number for each specimen is indicated. (**B**–**D**) Representative karyotypes from wild-type *TP53*$^{+/+}$ pig skin tissue (**B**), *TP53*$^{R167H/R167H}$ lymph node (**C**; case 5), and *TP53*$^{R167H/R167H}$ osteosarcoma (**D**; case 5) showing abnormal chromosome number and structures in the malignant cells.

later and plated on 64 96-well collagen-coated plates at a density of 200 cells/well. Selection was initiated 48 hours later with G418 (100 μg/ml). 10 days later, each infected cell plate was split among 3 96-well plates (1 for freezing, 1 for propagation, 1 to a PCR plate for immediate PCR screening). The freeze and propagation plates were returned to the incubator.

PCR screen and cell handling. Approximately 40% of wells contained live cell colonies following selection. Cells in the 96-well PCR plate were subjected to 5 μl lysis buffer (50 mM KCl, 1.5 mM $MgCl_2$, 10 mM Tris-Cl, pH 8.5, 0.5% Nonidet P40, 0.5% Tween, 400 μg/ml proteinase K) (69). Cell lysis plates were incubated at 65°C for 30 minutes, followed by 95°C for 10 minutes. The primers Screen F (NeoR), pTP53 PCR-R1, LDLR 5F, and LDLR-Exon5R1 were used to PCR amplify 2 μl lysate, with the following conditions: 95°C for 2 minutes; 30 cycles of 95°C for 20 seconds, 56°C for 20 seconds, and 68°C for 4.5 minutes; and finally 68°C for 7 minutes. The *LDLR* amplicon served as an internal control. The expected product for the targeted *TP53* allele was 1.9 kb and 4.3 kb for the LDLR product. The PCR-positive cells were grown to 100% confluence and either cryopreserved or expanded for the purpose of DNA isolation.

R167H-specific Southern blot. The PCR-positive PCR reactions were run on a 1.0% agarose gel, denatured in 0.5M NaOH and 1.5M NaCl for 20 minutes, and transferred to a positively charged nylon membrane (Roche) in 20× SSC overnight. The membrane was washed in 5× SSC for 5 minutes, air dried, and UV crosslinked. Detection of p53-R167H was achieved by Chemiluminescent Nucleic Acid Detection (Thermo Scientific) and a biotin-labeled probe. The membrane was prehybridized in 15 ml hybridization solution at 53.5°C. The DNA was hybridized with 15 μl (30 ng/μl) biotin-labeled probe, P53oligoprobe-3 (IDT DNA), for 90 minutes at 53.5°C. The membrane was washed in stringency wash buffer, then incubated in blocking buffer. HRP conjugate was added to the blocking buffer and incubated at 15 minutes at room temperature. The membrane was washed in wash buffer, then incubated in substrate equilibration solution. Finally, the membrane was incubated in luminol/peroxidase substrate and exposed to film (Kodak BioMax) for 1 second.

Southern blot. To validate PCR-positive cell lines, genomic DNA was isolated from the cells grown on propagation culture plates. 2–10 ng genomic DNA was used for whole genome amplification (Repli-G; Qiagen) and digested with AflII and EcoNI overnight. Following gel electrophoresis, samples were transferred to a positively charged nylon membrane (Roche) using an alkaline transfer procedure. The membrane was briefly rinsed in 5× SSC, completely dried, and subjected to UV crosslinking. The DNA probes for *TP53* and *Neo*^{R} were produced by PCR amplification using primers pTP53 Southern probe 3F/pTP53 Southern Probe 3R and PGK-NeoF/NeoR-R, respectively. Probes were labeled with α-^{32}P by random priming using Prime-a-Gene Labeling System (Promega), and the radioactive probes were purified using CHROMA SPIN+TE-100 columns (Clontech). Membranes were prehybridized in Rapid-hyb Buffer (GE Healthcare Life Sciences) for 30 minutes at 65°C, 25 μl of ^{32}P-labeled probe was added, and hybridization proceeded at 65°C for 2 hours. The membrane was washed in 2× SSC, 0.1% SDS, 1 time at room temperature for 20 minutes and in 0.1× SSC, 0.1% SDS, 3 times at 65°C for 15 minutes each. The membrane was exposed to film (Kodak BioMax MS) at –80°C overnight. For confirming animal genotype, high–molecular weight genomic DNA was isolated from pig umbilicus and digested with AflII and EcoNI. The remaining steps were performed as described above.

Genotyping of offspring from heterozygote crosses. Lysis of fresh pig umbilicus was achieved using a Direct Amp Kit (Denville Scientific). The lysate was diluted in 50% water, and 2 μl was directly added to a master mix containing primers PGK-F, P53 Geno 4F, and P53NeoExc. Screen 3R. PCR amplification was performed with the following reaction conditions: 95°C for 2 minutes; 35 cycles of 95°C for 10 seconds, 60°C for 10 seconds, and 68°C for 15 seconds; and finally 68°C for 3 minutes. The expected product for the targeted allele was 211 bp and that for the wild-type allele was 114 bp.

Nuclear transfer. Nuclear transfer was performed by Viagen Inc. as previously described (23). Briefly, *TP53*-targeted fetal fibroblasts were seeded in a 4-well plate and grown until contact inhibited. The cells were detached with trypsin and resuspended in salt-buffered NCSU-23 containing 10% FCS. Oocytes were matured in Earle's TC199-HEPES supplemented with 5 mg/ml insulin, 10 ng/ml EGF, 0.6 mM cysteine, 0.2 mM sodium pyruvate, 25 mg/ml gentamicin, 5 mg/ml FSH, and 10% porcine follicular fluid for 40 hours prior to manipulation.

Embryo transfer. Embryo transfer was performed at Exemplar Genetics. Briefly, reconstructed oocytes were transferred into synchronized postpubertal domestic gilts on the first day of standing estrus. Recipient gilts were preanesthetized with i.v. propofol (0.5–5 mg/kg), and anesthesia was maintained with inhaled isoflurane (3%–5% in oxygen via face mask). Following a midline incision to access the uterus, reconstructed embryos were transferred into the oviduct at the ampullary-isthmus junction. Intraoperative and postoperative analgesia was provided by i.m. injection of flunixin meglumine (2.2 mg/kg). Recipient animals were checked for pregnancy by abdominal ultrasound after day 21 and throughout gestation.

Checkpoint analyses in pig fibroblasts. Induction of the DNA damage checkpoint or senescence in response to oncogene activation was examined in pig fetal fibroblasts expressing wild-type p53 or mutant alleles of $TP53^{R167H}$ following treatment with a DNA-damaging agent or expression of mutant H-RAS^{G12V} protein, respectively. For the DNA damage response, early passage cells (P1–P3) were plated at 5×10^5 cells per 10-cm dish and treated with or without 0.4 μg/ml doxorubicin (Adriamycin) for 3 days. Cells were harvested, cell viability measured by trypan blue staining and counting on a hemacytometer, and samples were split for flow cytometric analysis of DNA content or Western blot analysis, exactly as described previously (70). Antibodies used in Western analyses were against p53 (Santa Cruz, sc-126 [DO-1], 1:200), p21 (BD Pharmingen, 554228, 1:100), and GAPDH (Abcam, Ab8245, 1:20,000). To assess senescence, early passage cells (P1–P4) were infected with pBabe-puro vector control or pBabe-H-RAS^{G12V}-puro retroviruses for 2 days, using methods of virus preparation and infection identical to those reported previously (71, 72). Infected cells were selected with 1 μg/ml puromycin for 2 days and replated at identical cell numbers; 5–8 days later, induction of senescence was measured by cell counting, quantitative RT-PCR for porcine *CDKN1A* mRNA expression, staining for SA-βgal activity (73), and phase-contrast microscopy. Semiquantitative RT-PCR for human H-RAS^{G12V} mRNA expression was performed as described previously (74) to verify its expression in infected cells.

RT-PCR. Total RNA was isolated (RNeasy kit, Qiagen) and synthesis of cDNA performed using the iScript cDNA Synthesis kit (Bio-Rad). Quantitative RT-PCR was performed using Power SYBR Green PCR Master Mix (Applied Biosystems) with data collected in triplicate from 3 independent experiments on CFX Connect Real Time System thermal cycler (Bio-Rad). Values were normalized to β-actin values, with relative expression calculated using a comparative Ct method (75). Primers used in RT-PCR reactions to measure human H-RAS^{G12V}, porcine *CDKN1A*, and porcine *ACTB* mRNA levels are listed in Supplemental Table 3.

Clinical evaluation. Pigs were monitored ≥2 times daily for clinical signs of morbidity by experienced animal care staff. Parameters that were monitored included, but were not limited to, loss of condition, lameness, reduced feed consumption, general morbidity, and enlarged peripheral lymph nodes. Additionally, peripheral blood was collected every 2 months for complete blood count (CBC) and chemistries. Clinical presentations of the affected cases are described in Supplemental Table 2.

Peripheral blood analysis. Peripheral blood samples were collected from pigs every 4–6 weeks to monitor for signs of clinical disease. Samples were submitted to a commercial laboratory (Marshfield Labs) for analysis.

Animal preparation for imaging. Pigs were transported to and from the University of Iowa on the day of the imaging procedure. All procedures were performed under anesthesia, induced with a mixture of telazol (2.2 mg/kg), ketamine (1.1 mg/kg), and xylazine (1.1 mg/kg) and maintained with 3%–5% isoflurane. Pigs were mechanically ventilated through intubation with a balloon cuffed 7–8 mm tracheal tube. Ventilation was performed at 100% oxygen with 5 cm H_2O positive end expiratory pressure (PEEP), tidal volume of 10 ml/kg, and an appropriate respiration rate to maintain an end-tidal (ET) CO_2 of 35–45 mmHg. Isoflurane anesthesia, ventilation, and forced inspiratory breath-holds of 20 cm H_2O were achieved throughout image data acquisition with a Primer SP MRI-Compatible Veterinary Anesthesia Ventilator (DRE Veterinary). Peripheral i.v. access was obtained via a 20-gauge ear vein cannula for administration of contrast and flushed with heparinized saline (500 U/l) to prevent unwanted blood clotting between administrations. After CT and MRI acquisition, animals were recovered.

CT acquisition. 4 CT datasets (noncontrast head, noncontrast chest-abdomen-pelvis, contrast chest, and contrast abdomen-pelvis) were acquired using a Somatom Definition Flash 128-multidector dual-source CT scanner (Siemens Healthcare). Noncontrast head CT (Spiral, 120 kV, 390 mAs, 1 s rotation time, pitch of 0.5, H31 reconstruction kernel, 0.5 mm slice thickness) was acquired to assess the skeletal structure and indicate whether a brain MRI was warranted. Noncontrast chest-abdomen-pelvis CT was acquired during an enforced inspiratory breath hold at 20 cm H_2O (Spiral, 120 kV, 210 mAs, 0.5 s rotation time, pitch of 1, B35 kernel, 0.5 mm slice thickness). The enforced breath-hold eliminated respiratory motion artifact and increased the diagnostic quality of the dataset acquired. Finally, for contrast CT, 2 ml/kg nonionic iodinated contrast was injected at 4 ml/s, with 15-s delay for thorax scan and 70-s delay for abdomen, both with enforced inspiratory breath-holds (Spiral, 120 kV, 210 mAs, 0.5 s rotation time, pitch of 1, B35 kernel, 0.5 mm slice thickness).

MRI acquisition. MRI data was obtained with a TIM Trio 3T MRI system (Siemens Healthcare). A high-resolution brain scan was obtained to assess brain tumors using a 3D turbo spin echo with variable flip angle (SPACE) protocol (TR/TE, 1,630/119 ms; flip angle, 120°; echo train length, 141; resolution, 0.86 mm × 0.86 mm × 0.9 mm slice thickness). An additional axial diffusion tensor imaging protocol (TR/TE, 2,800/83 ms; flip angle, 90°; resolution, 1.5 mm × 1.5 mm × 5 mm slice thickness) was performed for detailed analysis of the white matter. For the chest and abdomen, standard T2-weighted scans acquired in the axial (TR/TE, 4,293/156 ms; flip angle, 120°; echo train length, 109; resolution, 1.37 mm × 1.37 mm × 5 mm slice thickness) and coronal (TR/TE, 4,286/157 ms; flip angle, 120°; echo train length, 109; resolution, 1.48 mm × 1.48 mm × 5 mm slice thickness) planes were used to assess areas of atypical fluid content, such as metastatic tumors or areas of inflammation. Due to the increased scan time, motion artifact was eliminated using respiratory navigation. A volume interpolated breath hold examination (VIBE), T1-weighted 3D fast

gradient echo method, contrast-enhanced abdominal sequence (TR/TE, 4.34/1.9; flip angle, 12°; resolution, 1.37 mm × 1.37 mm × 3 mm slice thickness) was acquired precontrast and 30, 60, and 180 seconds after administration of 0.2 ml/kg gadolinium contrast (MultiHance, Bracco Diagnostics Inc.) injected through a peripheral ear vein. These scans were used to analyze blood flow through the liver and obtain greater anatomical detail of the abdomen. An additional postcontrast axial VIBE chest scan (TR/TE, 4.34/1.92; flip angle, 12°; resolution, 1.37 mm × 1.37 mm × 3 mm slice thickness) was acquired for additional anatomical detail of the lungs. Due to the short acquisition time with the VIBE scans, breath-holds at an inspiratory pressure of 20 cm H_2O were used to reduce motion artifact.

Radiological assessment. All image data was qualitatively evaluated by a radiologist with experience in porcine studies, using the OsiriX platform (76). Response Evaluation Criteria in Solid Tumors (RECIST) 1.1 was used to measure tumor and lymph node size (77). Segmentation and volumetric rendering of the osteogenic tumor in the mesentery was achieved using OsiriX threshold-based 3D region growing algorithm (threshold range, 250–2,000 HU).

Segmentation of the renal cell tumor at imaging time points 1 and 2 were achieved using tools from the Pulmonary Analysis Software Suite (PASS) (78). The contrast-enhanced venous phase (70-s delay) 3.0 mm, thick axial CT scans were analyzed with PASS. Total volume (in ml) as well as mean, SD, and coefficient of variation of the CT attenuation (in HU) were calculated from the segmented liver image. Using precontrast and postcontrast MRI sequences, the signal intensity of the tumor relative to that of the kidney was reported.

Liver and spleen were quantitatively assessed to determine the presence of lymphoma. Manually segmented liver organ volumes in the venous phase from contrast-enhanced CT scans were done using PASS. In addition to identifying the boundary of the organ, large internal vessels were segmented and excluded. Total volume (in ml) and mean and SD CT attenuation (in HU) were calculated from the segmented liver images. The dynamic perfusion heterogeneity of the liver and spleen were quantitatively assessed using the MRI abdominal VIBE sequence data, including precontrast and 30, 60, and 180 s postcontrast data acquisitions. PASS was used to obtain 3–4 square regions of interest (ROIs) within the liver, spleen, and flank muscle. Areas with prominent large vessels were excluded from the ROIs. Liver/muscle and spleen/muscle ratios were computed along with coefficient of variation to assess overall MRI signal intensity and heterogeneity.

Tissues. Euthanasia was performed according to Institutional Animal Care and Use Committee (IACUC) approval. Necropsy examination and tissue collection procedures were coordinated by a veterinary pathologist experienced with genetically modified porcine models. Lesions identified by imaging techniques were targeted for examination and tissue collection, and the remaining tissues were screened for lesions. Collected tissues were placed in appropriate volumes (>20:1 fixative/tissue) of 10% neutral buffered formalin for ~3–5 days. Formic acid (25%) was used to decalcify bony lesions/tumors. Samples were submitted to the Comparative Pathology Laboratory, Department of Pathology, University of Iowa, for standard tissue processing, embedding, and sectioning (~4 μm). Tissues were stained with H&E for general examination by the veterinary pathologist.

Molecular genetic analyses of $TP53^{R167H/R167H}$ tumors. Isolated tumors were quick frozen in liquid nitrogen for Western analyses or placed in F10 media containing 20% FCS for subsequent culturing and cytogenetic analysis. Frozen tumor sections were pulverized with a mortar and pestle, lysed in ice-cold RIPA lysis buffer (50 mM Tris, pH 8.0, 150 mM NaCl, 1 mM EDTA, 1% Triton X-100, 0.1% SDS, 0.5% sodium deoxycholate with protease and phosphatase inhibitors), and protein quantified by BCA analysis (Pierce). Equivalent amounts of protein (100 μg) from each sample were analyzed by SDS-PAGE and Western blotting using enhanced chemiluminescence for protein detection (ECL; Amersham). Antibodies used included those against p53 and GAPDH (see above) as well as cyclin B1 (Santa Cruz, sc-752, 1:200).

Chromosome analysis. Cell cultures were established from either wild-type pig skin fibroblasts or tumor cells derived from $TP53^{R167H/R167H}$ pigs. Cells were arrested in metaphase by adding ethidium bromide (final concentration, 12.5 μg/ml) for 40 minutes followed by colcemid (final concentration, 6 μg/ml). After 1–2 hours, cells were incubated for 25 minutes at room temperature with hypotonic solution (3:1 mixture of 0.8% sodium citrate and 0.075M potassium chloride). Cells were then fixed 3 times with 3:1 methanol/acetic acid. Chromosome spreading was performed on coverslips in a Thermotron chamber. Coverslips were mounted on glass slides after the drying process. 10–20 G-banded metaphases were analyzed. Karyotype images were captured using the CytoVision computerized imaging system (Applied Imaging).

Statistics. For measurement of SA-βgal–positive cells, data represent mean ± SD from 3 independent experiments, with statistical significance calculated by 2-way ANOVA. For peripheral blood analysis, values between nondiseased control and lymphoma cases were statistically analyzed using 2-way repeated-measures ANOVA and Bonferroni post-test. A P value less than 0.05 was considered significant.

Study approval. This study was carried out in accordance with the recommendations in the NIH *Guide for the Care and Use of Laboratory Animals*. All animals were developed and housed in the AAALAC-accredited facilities of Exemplar Genetics. Standard procedures for animal husbandry were used throughout. The IACUC of Exemplar Genetics and the University of Iowa approved all animal experiments. Imaging procedures were conducted at the University of Iowa in accordance with the IACUC-approved protocol.

Acknowledgments

This research was funded in part by Exemplar Genetics and the NIH via the University of Iowa Environmental Health Sciences Research Center (grant P30 ES005605), the Institute for Clinical and Translational Science (grant UL1 TR000442), and the Holden Comprehensive Cancer Center (grant P30 CA086862). This publication's contents are solely the responsibility of the authors and do not necessarily represent the official views of the NIH. We thank Daniel Thedens, Jered Sieren, Nicholas Stoyles, David Stoltz, Mahmoud Abou, Mark Hoegger, Brian Huedepohl, and Cara Haden as well as the Comparative Pathology Laboratory and the Shivanand R. Patil Cytogenetics and Molecular Laboratory for technical assistance. We also thank John Buatti, Frederick Domann, Aliasger Salem, Chuck Sherr, Martine Roussel, Lezlee Coghlan, Donna Kusewitt, and John Swart for helpful discussions.

Address correspondence to: Christopher S. Rogers, Exemplar Genetics, 2500 Crosspark Rd., Ste E126, Coralville, Iowa 52241, USA. Phone: 319.665.2664; Email: chris.rogers@exemplargenetics.com.

1. Siegel R, Naishadham D, Jemal A. Cancer statistics, 2012. *CA Cancer J Clin*. 2012;62(1):10–29.
2. Cheon DJ, Orsulic S. Mouse models of cancer. *Annu Rev Pathol*. 2011;6:95–119.
3. Ritman EL. Current status of developments and applications of micro-CT. *Annu Rev Biomed Eng*. 2011;13:531–552.
4. Won C, et al. CT-based assessment of regional pulmonary microvascular blood flow parameters. *J Appl Physiol (1985)*. 2003;94(6):2483–2493.
5. Chon D, Beck KC, Larsen RL, Shikata H, Hoffman EA. Regional pulmonary blood flow in dogs by 4D-X-ray CT. *J Appl Physiol (1985)*. 2006;101(5):1451–1465.
6. Dakin JH, Evans TW, Hansell DM, Hoffman EA. Regional pulmonary blood flow in humans and dogs by 4D computed tomography. *Acad Radiol*. 2008;15(7):844–852.
7. Alford SK, van Beek EJ, McLennan G, Hoffman EA. Heterogeneity of pulmonary perfusion as a mechanistic image-based phenotype in emphysema susceptible smokers. *Proc Natl Acad Sci U S A*. 2010;107(16):7485–7490.
8. Basel MT, et al. Human xenografts are not rejected in a naturally occurring immunodeficient porcine line: a human tumor model in pigs. *Biores Open Access*. 2012;1(2):63–68.
9. Flisikowska T, et al. A porcine model of familial adenomatous polyposis. *Gastroenterology*. 2012;143(5):1173–1175 e1171.
10. Leuchs S, et al. Inactivation and inducible oncogenic mutation of p53 in gene targeted pigs. *PLoS One*. 2012;7(10):e43323.
11. Levine AJ, Oren M. The first 30 years of p53: growing ever more complex. *Nat Rev Cancer*. 2009;9(10):749–758.
12. Vousden KH, Prives C. Blinded by the Light: The growing complexity of p53. *Cell*. 2009;137(3):413–431.
13. Vogelstein B, Lane D, Levine AJ. Surfing the p53 network. *Nature*. 2000;408(6810):307–310.
14. Lowe SW, Sherr CJ. Tumor suppression by Ink4a-Arf: progress and puzzles. *Curr Opin Genet Dev*. 2003;13(1):77–83.
15. Nichols KE, Malkin D, Garber JE, Fraumeni JF, Fraumeni JF Jr, Li FP. Germ-line p53 mutations predispose to a wide spectrum of early-onset cancers. *Cancer Epidemiol Biomarkers Prev*. 2001;10(2):83–87.
16. Petitjean A, et al. Impact of mutant p53 functional properties on TP53 mutation patterns and tumor phenotype: lessons from recent developments in the IARC TP53 database. *Hum Mutat*. 2007;28(6):622–629.
17. Freed-Pastor WA, Prives C. Mutant p53: one name, many proteins. *Genes Dev*. 2012;26(12):1268–1286.
18. Olive KP, et al. Mutant p53 gain of function in two mouse models of Li-Fraumeni syndrome. *Cell*. 2004;119(6):847–860.
19. Kuperwasser C, et al. Development of spontaneous mammary tumors in BALB/c p53 heterozygous mice. A model for Li-Fraumeni syndrome. *Am J Pathol*. 2000;157(6):2151–2159.
20. Lang GA, et al. Gain of function of a p53 hot spot mutation in a mouse model of Li-Fraumeni syndrome. *Cell*. 2004;119(6):861–872.
21. Hill KA, et al. Most spontaneous tumors in a mouse model of Li-Fraumeni syndrome do not have a mutator phenotype. *Carcinogenesis*. 2006;27(9):1860–1866.
22. Rogers CS, et al. Disruption of the CFTR gene produces a model of cystic fibrosis in newborn pigs. *Science*. 2008;321(5897):1837–1841.
23. Walker SC, et al. A highly efficient method for porcine cloning by nuclear transfer using in vitro-matured oocytes. *Cloning Stem Cells*. 2002;4(2):105–112.
24. Wu X, Bayle JH, Olson D, Levine AJ. The p53-mdm-2 autoregulatory feedback loop. *Genes Dev*. 1993;7(7A):1126–1132.
25. Senturk E, Manfredi JJ. Mdm2 and tumorigenesis: evolving theories and unsolved mysteries. *Genes Cancer*. 2012;3(3-4):192–198.
26. Lane DP. p53, guardian of the genome. *Nature*. 1992;358(6381):15–16.
27. Dittmer D, et al. Gain of function mutations in p53. *Nat Genet*. 1993;4(1):42–46.
28. Serrano M, Lin AW, McCurrach ME, Beach D, Lowe SW. Oncogenic ras provokes premature cell senescence associated with accumulation of p53 and p16INK4a. *Cell*. 1997;88(5):593–602.
29. Hussain SP, Schwank J, Staib F, Wang XW, Harris CC. TP53 mutations and hepatocellular carcinoma: insights into the etiology and pathogenesis of liver cancer. *Oncogene*. 2007;26(15):2166–2176.
30. Lee WK, Lau EW, Duddalwar VA, Stanley AJ, Ho YY. Abdominal manifestations of extranodal lymphoma: spectrum of imaging findings. AJR. *AJR Am J Roentgenol*. 2008;191(1):198–206.
31. Leite NP, et al. Cross-sectional imaging of extranodal involvement in abdominopelvic lymphoproliferative malignancies. *Radiographics*. 2007;27(6):1613–1634.
32. Treuting PM, Albertson TM, Preston BD. Case series: acute tumor lysis syndrome in mutator mice with disseminated lymphoblastic lymphoma. *Toxicol Pathol*. 2010;38(3):476–485.
33. Vogel P, Pletcher JM, Liang Y. Spontaneous acute tumor lysis syndrome as a cause of early deaths in short-term carcinogenicity studies using $p53^{+/-}$ mice. *Vet Pathol*. 2010;47(4):719–724.
34. McBride A, Westervelt P. Recognizing and managing the expanded risk of tumor lysis syndrome in hematologic and solid malignancies. *J Hematol Oncol*. 2012;5:75.
35. Schifter T, Cohen A, Lewinski UH. Severe tumor lysis syndrome following splenic irradiation. *Am J Hematol*. 1999;60(1):75–76.
36. Gylys-Morin V, Hoffer F, Kozakewich H, Shamberger R. Wilms tumor and nephroblastomatosis: imaging characteristics at gadolinium-enhanced MR imaging. *Radiology*. 1993;188(2):517–521.
37. Stanhope-Baker P, Kessler PM, Li W, Agarwal ML, Williams BR. The Wilms tumor suppressor-1 target gene podocalyxin is transcriptionally repressed by p53. *J Biol Chem*. 2004;279(32):33575–33585.
38. Ordonez N, Rosai J. Urinary tract. In: Rosai J, ed. *Rosai and Ackeman's Surgical Pathology*. New York, New York, USA: Mosby; 2004.
39. Brachova P, Thiel KW, Leslie KK. The consequence of oncomorphic TP53 mutations in ovarian cancer. *Int J Mol Sci*. 2013;14(9):19257–19275.
40. Ciriello G, Miller ML, Aksoy BA, Senbabaoglu Y, Schultz N, Sander C. Emerging landscape of oncogenic signatures across human cancers. *Nat Genet*. 2013;45(10):1127–1133.
41. Coussens LM, Werb Z. Inflammation and cancer. *Nature*. 2002;420(6917):860–867.
42. Kalluri R, Zeisberg M. Fibroblasts in cancer. *Nat Rev Cancer*. 2006;6(5):392–401.
43. Sieren JC, et al. An automated segmentation approach for highlighting the histological complexity of human lung cancer. *Ann Biomed Eng*. 2010;38(12):3581–3591.
44. Shiao SL, Ganesan AP, Rugo HS, Coussens LM. Immune microenvironments in solid tumors: new targets for therapy. *Genes Dev*. 2011;25(24):2559–2572.
45. Frangioni JV. New technologies for human cancer imaging. *J Clin Oncol*. 2008;26(24):4012–4021.
46. Simons D, Kachelriess M, Schlemmer HP. Recent developments of dual-energy CT in oncology. *Eur Radiol*. 2014;24(4):930–939.
47. Sharma R, Aboagye E. Development of radiotracers for oncology — the interface with pharmacology. *Br J Pharmacol*. 2011;163(8):1565–1585.
48. Shiga T, et al. A new PET scanner with semiconductor detectors enables better identification of intratumoral inhomogeneity. *J Nucl Med*. 2009;50(1):148–155.
49. Weissleder R. Scaling down imaging: molecular mapping of cancer in mice. *Nat Rev Cancer*. 2002;2(1):11–18.
50. Bowen SR, et al. Challenges and opportunities in patient-specific, motion-managed and PET/CT-guided radiation therapy of lung cancer: review and perspective. *Clin Transl Med*. 2012;1(1):18.
51. Birch JM, et al. Prevalence and diversity of constitutional mutations in the p53 gene among 21 Li-Fraumeni families. *Cancer Res*. 1994;54(5):1298–1304.
52. Kleihues P, Schauble B, zur Hausen A, Esteve J, Ohgaki H. Tumors associated with p53 germline mutations: a synopsis of 91 families. *Am J Pathol*. 1997;150(1):1–13.
53. Porter DE, Holden ST, Steel CM, Cohen BB, Wallace MR, Reid R. A significant proportion of patients with osteosarcoma may belong to Li-Fraumeni cancer families. *J Bone Joint Surg Br*. 1992;74(6):883–886.
54. Jacobs R, Messick J, VAlli V. Tumors of the hematopoietic system. In: *Tumors In Domestic Animals*. Ames, Iowa, USA: Iowa State Press; 2002:159–160.
55. Migaki G, Nelson LW, Todd GC. Prevalence of embryonal nephroma in slaughtered swine. *J Am Vet Med Assoc* 1971;159(4):441–442.
56. Miller CW, et al. Frequency and structure of p53 rearrangements in human osteosarcoma. *Cancer Res*. 1990;50(24):7950–7954.
57. Tsuchiya T, Sekine K, Hinohara S, Namiki T, Nobori T, Kaneko Y. Analysis of the p16INK4, p14ARF, p15, TP53, and MDM2 genes and their prognostic implications in osteosarcoma and Ewing sarcoma. *Cancer Genet Cytogenet*. 2000;120(2):91–98.
58. Wunder JS, et al. TP53 mutations and outcome in osteosarcoma: a prospective, multicenter study. *J Clin Oncol*. 2005;23(7):1483–1490.
59. Luetke A, Meyers PA, Lewis I, Juergens H. Osteosarcoma treatment — where do we stand? A state of the art review. *Cancer Treat Rev*. 2014;40(4):523–532.
60. Radig K, Schneider-Stock R, Mittler U, Neumann

HW, Roessner A. Genetic instability in osteoblastic tumors of the skeletal system. *Pathol Res Pract*. 1998;194(10):669–677.
61. Dal Cin P, Sciot R, Samson I, De Wever I, Van den Berghe H. Osteoid osteoma and osteoblastoma with clonal chromosome changes. *Br J Cancer*. 1998;78(3):344–348.
62. Oliveira CR, et al. Classical osteoblastoma, atypical osteoblastoma, and osteosarcoma: a comparative study based on clinical, histological, and biological parameters. *Clinics*. 2007; 62(2):167–174.
63. Unni K. *Dahlin's Bone Tumors: General Aspects and Data on 11,087 Cases*. Philadelphia, Pennsylvania, USA: Lippencout-Raven; 1996.
64. Walkley CR, et al. Conditional mouse osteosarcoma, dependent on p53 loss and potentiated by loss of Rb, mimics the human disease. *Genes Dev*. 2008;22(12):1662–1676.
65. Hingorani SR, et al. Trp53R172H and KrasG12D cooperate to promote chromosomal instability and widely metastatic pancreatic ductal adenocarcinoma in mice. *Cancer Cell*. 2005; 7(5):469–483.
66. Jackson EL, et al. The differential effects of mutant p53 alleles on advanced murine lung cancer. *Cancer Res*. 2005;65(22):10280–10288.
67. Lai L, Prather RS. Production of cloned pigs by using somatic cells as donors. *Cloning Stem Cells*. 2003;5(4):233–241.
68. Pomp D, Good BA, Geisert RD, Corbin CJ, Conley AJ. Sex identification in mammals with polymerase chain reaction and its use to examine sex effects on diameter of day-10 or -11 pig embryos. *J Anim Sci*. 1995;73(5):1408–1415.
69. McCreath KJ, Howcroft J, Campbell KHS, Colman A, Schnieke AE, Kind AJ. Production of gene-targeted sheep by nuclear transfer from cultured somatic cells. *Nature*. 2000;405(6790):1066–1069.
70. Muniz VP, et al. RABL6A promotes oxaliplatin resistance in tumor cells and is a new marker of survival for resected pancreatic ductal adenocarcinoma patients. *Genes Cancer*. 2013;4(7–8):273–284.
71. Modestou M, Puig-Antich V, Korgaonkar C, Eapen A, Quelle DE. The alternative reading frame tumor suppressor inhibits growth through p21-dependent and p21-independent pathways. *Cancer Res*. 2001;61(7):3145–3150.
72. Huang J, et al. RGS6 suppresses Ras-induced cellular transformation by facilitating Tip60-mediated Dnmt1 degradation and promoting apoptosis [published online ahead of print September 2, 2013]. *Oncogene*. doi:10.1038/onc.2013.324.
73. Rokudai S, Laptenko O, Arnal SM, Taya Y, Kitabayashi I, Prives C. MOZ increases p53 acetylation and premature senescence through its complex formation with PML. *Proc Natl Acad Sci U S A*. 2013;110(10):3895–3900.
74. Adam SJ, Rund LA, Kuzmuk KN, Zachary JF, Schook LB, Counter CM. Genetic induction of tumorigenesis in swine. *Oncogene*. 2007;26(7):1038–1045.
75. Pfaffl MW. A new mathematical model for relative quantification in real-time RT-PCR. *Nucleic Acids Res*. 2001;29(9):e45.
76. Rosset A, Spadola L, Ratib O. OsiriX: an open-source software for navigating in multidimensional DICOM images. *J Digit Imaging*. 2004;17(3):205–216.
77. Eisenhauer EA, et al. New response evaluation criteria in solid tumours: revised RECIST guideline (version 1.1). *Eur J Cancer*. 2009;45(2):228–247.
78. Guo J, Fuld MK, Alford SK, Reinhardt JM, Hoffman EA. Pulmonary Analysis Software Suite 9.0: Integrating quantitative measures of function with structural analyses. In: Brown M, et al., eds. *1th International Conference on Medical Image Computing and Computer Assisted Intervention, Pulmonary Image Analysis Workshop*. New York, New York, USA: CRC Press; 2008:283–292.